Global Ionizing Radiation Environment Mapping Using Starlink Satellite Data

Hamil Shah, *Member, IEEE*, Russell Van Cleave, William McAlpine, Zachary E. Fleetwood, Kim-Thu Pham *Member, IEEE*, Scott Shermer *Member, IEEE*

Abstract—We demonstrate the use of over 5,000 commercial-off-the-shelf complementary metal-oxide-semiconductor (CMOS) image sensors and simple total ionizing dose (TID) circuits from the Starlink satellite constellation to measure ionizing radiation effects in a low Earth orbit (LEO) environment with high spatial and temporal resolution. The constellation's main operating environment was modeled, ground tests were performed on the CMOS image sensor (CIS) and TID circuit, and on-orbit data were collected and analyzed from nearly 3,000 satellites in the primary 53 degree inclination shell. The estimated total ionizing dose and bright spot counts are compared to model predictions and known low-Earth orbit phenomena, respectively. The constellation of total ionizing dose circuits provides high confidence in design margin against cumulative dose risk. Data on single event effects in CIS are collected and shown to be capable of mapping high radiation regions of the orbit, such as the South Atlantic Anomaly. In total, this study demonstrates that thousands of low cost and readily available sensors hosted on mega-constellations can potentially inform future models by supplementing external data as a source of near real-time measurements of the radiation environment in LEO.

Index Terms—complementary metal-oxide-semiconductor (CMOS), CMOS image sensor (CIS), commercial-off-the-shelf (COTS), device under test (DUT), low Earth orbit (LEO), South Atlantic Anomaly (SAA), single event effects (SEE), solar particle event (SPE), total ionizing dose (TID)

I. INTRODUCTION

OVER the last decade, a number of satellite mega-constellation designs have been proposed for Low-Earth Orbit (LEO) [1,2]. A primary concern for building these systems lies in creating performant, reliable, and low-cost spacecraft while maintaining space safety. To achieve this, designers and operators must be acutely aware of the risks of space radiation effects in their orbital environment. This becomes particularly challenging for manufacturing spacecraft at a scale when price per component is a key design constraint. Engineers must frequently opt for cheap commercial-off-the-shelf (COTS) components which can be purchased at a fraction of the cost of radiation-hardened alternatives [3]. This approach requires a critical understanding of the operational environment and the associated radiation risk to spacecraft avionics. Similarly, the aforementioned component, system, and environment level knowledge is crucial to inform potential

mitigations for increased solar activity and for understanding anomalies [4].

The desire to understand the radiation environment has motivated previous similar studies. The Responsive Environmental Assessment Commercially Hosted payload project (REACH), the Active Magnetospheric and Planetary Electrodynamics Response Experiment (AMPERE) and the Project for OnBoard Autonomy - Vegetation (PROBA-V) are three examples of efforts to collect near-real-time data on the space environment [5–7]. These projects have utilized either custom-designed sensors (operating as a hosted payload) or existing sensors designed into constellation spacecraft that can characterize magnetic field strength or particle flux over a range of energies. However, studies of this kind are often limited to no more than a few dozen spacecraft resulting in constrained revisit rates for any given geophysical location.

In contrast, the primary benefit of the Starlink constellation sensor implementations resides in the spatiotemporal data resolution enabled by its unprecedented scale. Starlink constellation sensors considered for this study collected over 20 device-years of data every day with a revisit rate of less than five minutes for any point along the orbital path. This method of data collection is complementary to environment data collected with higher fidelity sensors. Furthermore, the quantity of samples gathered is statistically significant enough to bound environment data with higher confidence.

The purpose of this work is to discuss how Starlink – designed, manufactured, and launched by SpaceX – is able to use simple on-board sensors to capture near real-time data on the space radiation environment and how those effects are modeled in the constellation's primary orbital shell. A model of a Starlink satellite is shown in Figure 1 for reference. Starlink currently has over 4,000 satellites in operation, with the majority operating at an altitude of approximately 550 km and an inclination of 53 degrees [1]. Specifically, this work presents on-orbit data from approximately 8,000 active radiation sensors in the Starlink constellation. The sensors used in Starlink satellites consist of both a custom total ionizing dose (TID) sensor and a complementary metal-oxide-semiconductor (CMOS) image sensor which are installed onboard every vehicle. Each satellite has four identical copies of the TID sensor and two identical copies of the CMOS image sensor (CIS).

In this paper, TID sensor data is compared to cumulative dose predictions generated with an environment and shielding model. Single event effects (SEE) detected in the image sensor are compared against known environmental effects.
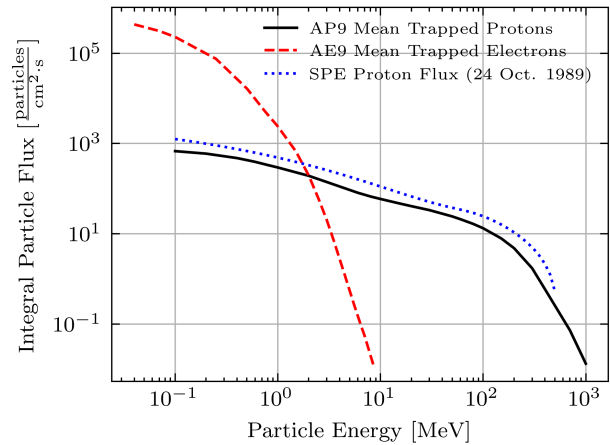
Fig. 1. Starlink Satellite Model

Fig. 2. IRENE-AE9/AP9 (v1.50.001) Integral Particle Spectra and Solar Particle Flux for Starlink Satellites in a 550km circular orbit at 53 degrees inclination

First, the modeling of Starlink's main operational environment and analysis used to inform mission performance is discussed. Second, the relevant sensor details and the ground test characterization of their radiation response are briefly discussed. Finally, the captured on-orbit data from TID sensors are compared against the environmental model and the captured CIS data is compared against known dependencies in location and measurements from other spacecraft over time.

II. DESIGN AND ANALYSIS DETAILS

A. Starlink Environment Modeling

To inform radiation environment design risk for Starlink satellites, the trapped proton and electron radiation environments were modeled using the International Radiation Environment Near Earth (IRENE) AE9/AP9 (v1.50.001), a space radiation environment modeling tool available from the Air Force Research Laboratory [8]. Specifically, the mean trapped electron and proton models in IRENE were used to derive the trapped belt protons and electrons, shown in Figure 2, for Starlink satellites operating at an inclination of 53 degrees in a 550 km circular orbit. The mean trapped proton belt flux in the mission environment was then used to get a baseline expectation for flux readings during quiet solar conditions. It was assumed that the trapped environment mean AP9/AE9 mission fluences could be sufficiently scaled for repeated ground tracks using the modeled spectra. The Space Environment Information System (SPENVIS) program was leveraged to generate a solar proton flux model for the Starlink orbit using a mean composition of the flux at the spacecraft from the 24 October 1989 portion of the Xapsos model [9,10]. This model was derived using the "Størmer with eccentric dipole method", as described by Størmer in [11], to account for geomagnetic shielding. The geomagnetically shielded exterior solar proton flux used for the analysis is also included in Figure 2.

The SEE risk from Galactic Cosmic Rays (GCR), Van Allen belt protons, and solar proton spectra were transported through shielding provided by the satellite structure as part of the analysis for system level SEE rate predictions. However, the SEE impacts on the CMOS image sensors due to GCRs were negligible compared to the contribution from trapped belt protons. Nonetheless, the GCR model implemented for the system-level SEE analysis was the Cosmic Ray Effects on Micro-Electronics (CREME) 96 heavy-ion model, also using the Størmer magnetic cutoff, under quiet conditions for ions from atomic number (Z) equal to 1 to Z equal to 92 in Outil de Modélisation de l'Environnement Radiatif Externe (OMERE) [12,13]. The geomagnetic cutoff informs the threshold particle energy needed to penetrate the magnetosphere and reach the 550 km mission altitude and an assumed spherical shielding thickness of 1 g/cm^2 was used for the environment linear energy transfer (LET) spectrum generation.

The FASTRAD radiation transport software from TRAD was used to calculate the cumulative dose for the TID sensors and to derive a transported proton spectrum for CMOS image sensors for their respective physical locations within the vehicle [14]. A FASTRAD reverse Monte Carlo (RMC) TID analysis was performed for the four TID sensor locations onboard the satellite using the particle spectra shown in Figure 2. The predicted average TID sensor dose rates ranged from 0.33 and 0.74 rad(SiO$_2$)/day, depending on location. A shielding distribution for the CIS was generated with a ray-trace calculation as shown in Figure 3. The shielding thicknesses in the histogram below were cross-referenced to the Planetary Science and Technology from Analog Research (PSTAR) program lookup tables for aluminum [15]. The results indicate that the typical threshold energy necessary for a proton to reach the image sensor is approximately 55 MeV based on the shielding distribution with a minimum of approximately 35 MeV.

B. Total Ionizing Dose Sensor

The TID sensor is a low voltage, low power draw (200 mW), small form factor device which provides temperature-
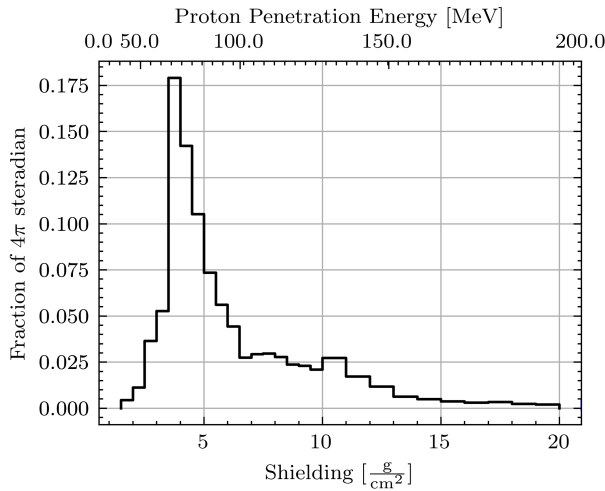
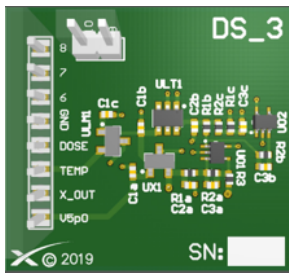Fig. 3. Fractional Distribution of Proton Penetration Thresholds for the Starlink CMOS Imager

Fig. 4. Test card used for calibration of dose sensor readings.

compensated output voltage that linearly scales with dose from 0 to 2 krad(SiO_2). The upper range on the sensor was selected based on environment modeling which showed that no sensor should receive more than 2 krad(SiO_2) over a five year span. Internally, dose sensors were calibrated against gamma sources at multiple dose rates and proton energies. Gamma test results are reported. A total of four design samples were irradiated and characterized using terrestrial gamma ray sources with two samples tested at a low dose rate of 0.2 rad(SiO_2)/s and two samples tested at a high dose rate of 2 rad(SiO_2)/s. An example test card render is shown in Figure 4. Results from testing show that the TID sensor increases 1 mV in output voltage for every 0.387 rad(SiO_2) of total dose. Annealing up to temperatures of 100 °C has a negligible impact on output voltage with less than 1% variance before and after exposure. While the specific components used for the dose sensor design are proprietary to SpaceX, a similar approach to recreate these results is achievable by purchasing, flying, and monitoring commercially available radiation dose sensors such as the Teledyne μDOS-001 [16]. However, use of a similarly high accuracy sensor introduces greater challenges with respect to cost and availability. Consequently, a decision to use a custom SpaceX dosimeter made with readily available COTS components was pursued to comply with cost, production, and schedule needs while providing useful information for constellation planning and operations.

Fig. 5. CMOS imager under high proton flux irradiation

C. CMOS Image Sensor

CMOS image sensor (CIS) radiation effects have been extensively studied [17–21]. Therefore, the key tests for the CIS on-board Starlink were performed to ensure it was capable of meeting availability and total lifetime requirements. Tests were performed to observe single event effects in response to energetic protons and to characterize the response to total ionizing dose.

1) Single Event Effects: Incident particles may deposit high charge in a small group of pixels or in a track and show up in captured images as 'bright spots' when viewed against a dark frame [18]. In many cases, the bright spots clear as the pixels are read, but in some cases bright spots persisting across frames (stuck pixels) may occur which require a power-cycle of the device or may not anneal in a reasonable time. Controller errors including full rows of bright pixels were expected and could be resolved with a power cycle of the CMOS image sensor.

The CMOS image sensor was characterized and tested at multiple proton beam facilities, incidence angles, exposure time, and energy levels of 30, 50, 75 and 200 MeV. The results shown in this study utilize data available from a 200 MeV proton test where the unit was taken to a total fluence of 1.06×10^{10}. The test setup utilized an evaluation board for the device under test (DUT) with shielding for the circuitry surrounding the active pixel sensor (APS), a power supply for the DUT evaluation board, and a laptop with vendor-supplied software to communicate to the DUT and capture images (with 22 ms exposure time) during irradiation. The DUT was also covered so that nominal image captures were dark, and any stray light in the beam room would not affect the results. The DUT was tested in a series of proton exposure periods using a commercial evaluation board and custom software. Figure 5 shows an image capture during irradiation.

In agreement with other studies of CMOS image sensors [18], bright spot accumulation was observed at a rate proportional to the proton flux of the beam, and the total number of un-clearable stuck pixels correlated with the total DUT fluence. These trends are illustrated in Figure 6 and Figure 7
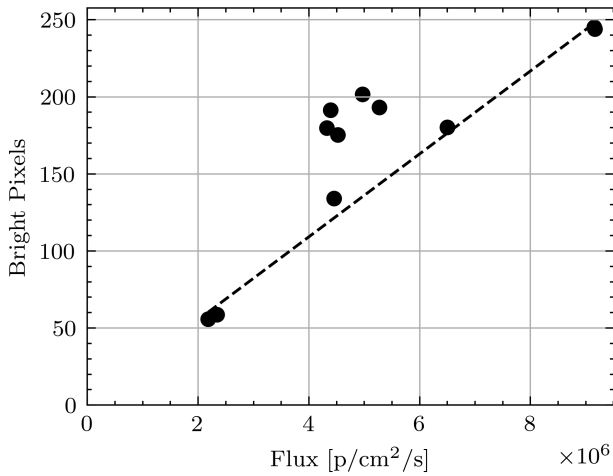
Fig. 6. Bright pixels vs. 200 MeV proton beam flux
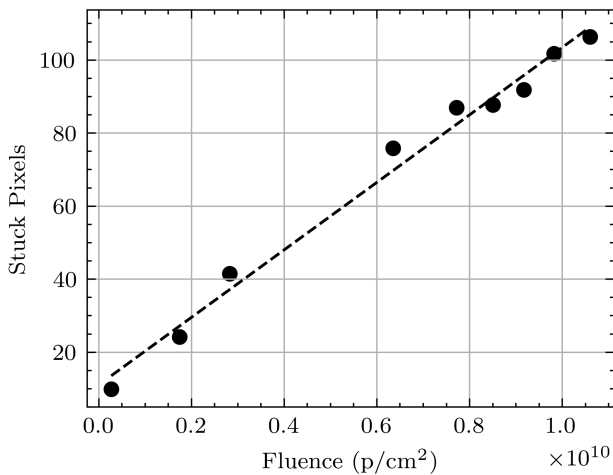

Fig. 8. Mean Pixel Value vs. Temperature

Fig. 7. Stuck pixels vs. total DUT 200 MeV proton fluence

respectively, with the line being fitted using the least squares method. Potential outliers were removed from the fit of data on bright pixels vs. flux. From the least squares fit to data representing bright pixels vs. flux, there was an increase of approximately 2.68×10^{-5} bright pixels per unit increase in flux (particle per square centimeter per second) with a baseline of approximately 1.6 bright pixels at zero flux. The baseline of 1.6 bright pixels is unexpected, but may be due to any combination of sensor noise, outliers in the data, or insufficient samples at each level of flux. Future tests should attempt to calibrate for any potential noise by including a measurement prior to irradiation, and capture more data at each level of flux. The least squares fit to data representing stuck pixels vs. fluence indicates there was an increase of approximately 9.24×10^{-9} stuck pixels per unit increase in fluence (particles per square centimeter) with a baseline of 1.1 stuck pixels at zero fluence.

2) Total Ionizing Dose: In addition to the single event effects observed on CIS, total ionizing dose can affect imager performance. The image sensor was tested in a Cobalt-60 source facility to characterize imager changes as a function
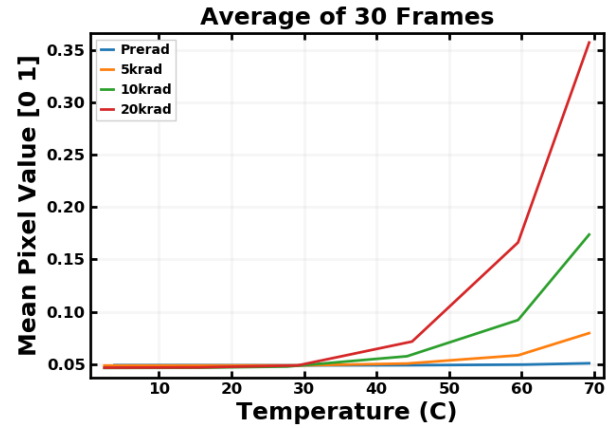
of dose. The test recorded current drawn by the imager and frames from the imager to understand the dark current increase as a function of dose. The test was performed at a dose rate of 2.49 rad(SiO_2)/s with measurements taken at 5 krad(SiO_2), 10 krad(SiO_2), and 20 krad(SiO_2). At each step, characterization was performed across temperature at 0 °C, 15 °C, 30 °C, 45 °C, 60 °C, and 70 °C with 30 light frame and 30 dark frames each. Exposure and gain settings were held constant throughout the test.

For Starlink, environment analysis has indicated that the total ionizing dose expected for the CMOS image sensors is approximately 0.5 krad(SiO_2) for the mission duration of 5 years. Further, to correct for longer-term effects in the imager and reduce noise in captured frames, a filter was developed to subtract the fixed pattern noise (FPN) of the imager. If necessary, operators can also take action to increase the temperature of the CIS in order to more quickly reverse defects and restore performance of imagers [22].

As desired, TID results indicated little shift in the mean value of pixels at a cumulative dose of 5 krad(SiO_2) at the expected operational temperatures. This is shown in Figure 8 where the difference between the mean pixel value of the dark frames captured pre-irradiation and following 5 krad(SiO_2) total dose exposure are not significantly different up to a temperature limit of 50 °C. TID was not considered a significant factor in measurement error with regard to bright spots, based on the expected mission dose and minimal shift in mean pixel value below 5 krad(SiO_2).

III. ON-ORBIT RESULTS

A. Total Ionizing Dose Sensor

Data were analyzed across Starlink satellites from January 28, 2022 to January 28, 2023 to compare 1-year of measured on-orbit dose against environment modeling predictions. Data were collected from up to 4 TID sensors per satellite with 2,526 sensors in total. Of note, the 1-year change in dose was utilized (as opposed to total reported dose) in order to account for the differences in time spent at operational altitudes. In order to be considered valid for the dataset, the satellite was
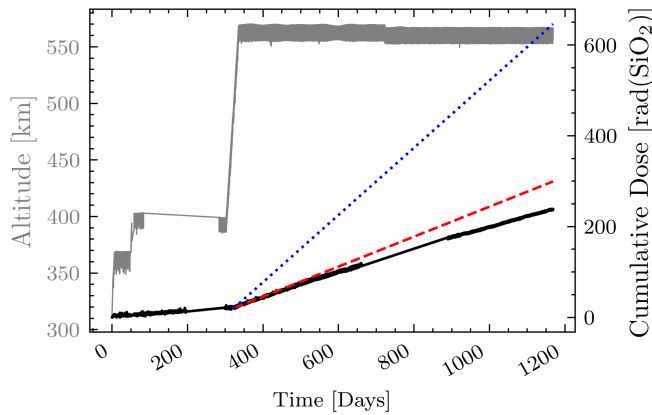
Fig. 9. Measurements from a TID sensor (black) and altitude (grey) from a Starlink satellite alongside on-station dose rate estimates for the high-dose rate sensor location (blue) and the low dose rate sensor location (red).

required to be at an operational altitude of 525 km or greater for the entire time span.

The estimated dose and altitude of a satellite was also calculated to verify the dependence of dose rate on space-craft altitude in LEO. Results show that the average 1 year cumulative dose for all valid sensors was 90 rad(SiO_2) with a standard deviation of 5.1 rad(SiO_2). To a first order, each TID sensor on the Starlink satellite accumulates approximately 0.25 rad(SiO_2)/day. Some difference in average dose rate is expected due to TID sensor location. Figure 9 shows results for a single TID sensor on a satellite with a delayed orbit raise alongside the predicted dose after the satellite reaches the operational altitude. Note the change in dose rate as the satellite raises. This satellite accumulated approximately 0.1 rad(SiO_2)/day before orbit raise and 0.27 rad(SiO_2)/day after orbit raise.

A FASTRAD reverse Monte-Carlo shielding analysis was performed for the four TID sensor locations on the satellite [14]. The satellite mass model was derived from an exported CAD model and accounted for 92% of the dry mass of the satellite. The predicted dose rate for the TID sensors ranged from 0.33 rad(SiO_2)/day to 0.74 rad(SiO_2)/day. This is a factor of 1.3 to 3 higher than the observed dose rates in the TID sensors. The TID analysis used the AP9 mean environment which is known to over predict LEO dose [23]. The empirical measurements coupled with characterization data for the TID sensor provide high confidence in the on-orbit TID rate. Further analysis using a higher fidelity vehicle mass model could be performed to investigate differences between predicted and observed dose rates. This analysis remains an item for future work.

B. CMOS Image Sensor

For this experiment, data were collected from December 1, 2022 to January 15, 2023 across all Starlink satellites that were in the main operational shell of approximately 53 deg. inclination and 550 km altitude. In total, data were collected from the two CIS onboard 2,914 Starlink satellites for a total of 5,828 CIS. Data were filtered to exclude satellites with

TABLE I
1-YEAR MEAN AND STANDARD-DEVIATION OF TID SENSORS ON STARLINK

Sensor	Mean Dose [rad(SiO_2)]	Standard Deviation [rad(SiO_2)]
#1	92.67	4.18
#2	88.47	4.90
#3	88.7	4.87
#4	90.52	5.18

CIS faults causing out-of-family measurements during the time period.

An algorithm to detect bright spots was developed for the CIS and data were stored on-board each respective Starlink satellite. This algorithm is similar to others previously demonstrated using clustering of pixels to detect single-event effects and ionizing radiation impacts to CIS [17]. On Starlink, an algorithm was written to estimate the number of transient bright spots based on frame subtraction. The algorithm estimated the number of bright spots per second, and this value was collected once a minute from all possible CIS across Starlink satellites. Earth-centered earth-fixed (ECEF) position data were also captured for each satellite and able to be converted to latitude, longitude, and altitude (LLA) for ease of plotting data onto two dimensional maps. Data were filtered to exclude several factors: temporary CIS faults, presence of stray light sources such as the sun and moon in the image, measurements taken in vehicle maneuver states, and measurements taken outside the operational altitude. In order to filter out such cases, a simple heuristic was derived such that the error between the two sensors on a satellite was less than 100% (relative to the lowest sensor).

A sample of the bright spot data collected from both sensors on a single satellite is shown in Figure 10 alongside a boolean flag to indicate when the satellite passed through the South Atlantic Anomaly (where the boolean indicates the satellite was within 3,500 km of -29° latitude and -40° longitude at the operational altitude). The repeated and varying duration of the boolean is explained by the orbit control of the satellite. At the on-station altitude, a single satellite completes one rotation around Earth in approximately 90 minutes. The ground track (2-D projected latitude / longitude) for a single satellite shifts by a small amount such that it does not cover the exact same latitude-longitude cell due to the relative rotation of Earth.

To visualize behavior across the whole constellation, data were converted to standard deviations from the mean over the total 48 hour period. Figure 11 shows a heatmap of all the data collected over ten minutes with intensity corresponding to the standard deviation value. By then plotting the top 5% of points in the ten minute window and the overall 48 hour window in Figure 12, we find that the changes in bright pixels occur predominantly while satellites are over the SAA, as expected in LEO. When compared to the shorter ten minute window of data, the data representing the full 48 hours distinctly defines the region of interest and the intensity of the environment when compared to other regions of the Starlink orbit.

The data from 1 December 2022 to 18 December 2022 (inclusive) were plotted in Figure 13. Note the clear separation
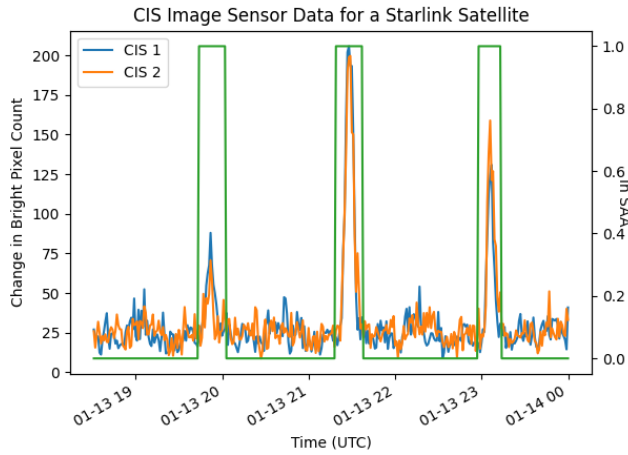
Fig. 10. On Orbit Data: CIS bright pixel telemetry from a single Starlink satellite (blue, orange) with a flag (green) to indicate satellite was passing through the South Atlantic Anomaly.
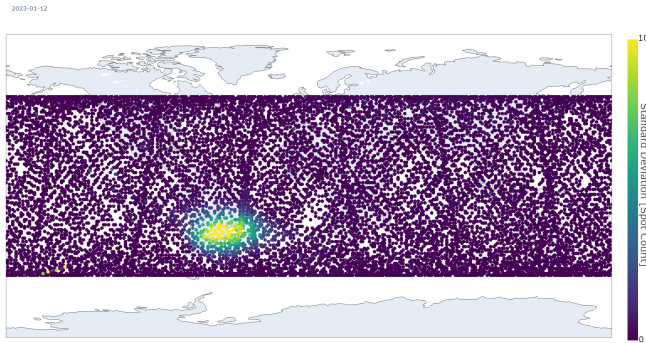

Fig. 11. On Orbit Data: CIS bright pixel measurements from 10 minutes starting 12 January 2023 (UTC) colored by standard deviation.
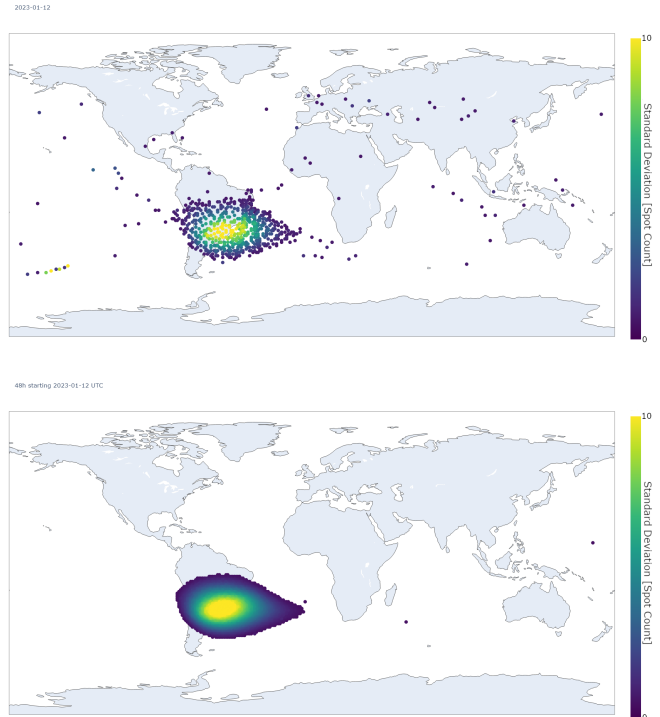

Fig. 12. On Orbit Data: Top 5% of CIS bright pixel measurements from 10 minutes (top) and 48 hours (bottom) starting 12 January 2023 (UTC) colored by standard deviation.
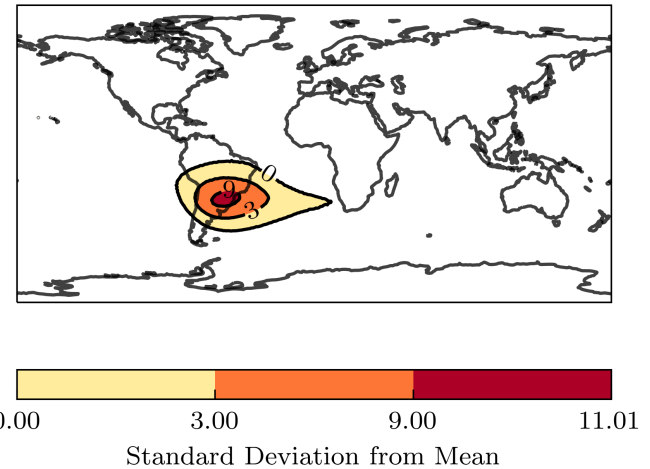

Fig. 13. Contours indicating latitude and longitude cells with data greater than 0, 3, and 9 standard deviations from global mean

between the SAA and the rest of the 53 degree inclination data. After filtering down values, each latitude and longitude cell had averaged data from least 136 satellites (272 CMOS image sensors), and higher latitudes where satellites spend more time had up to 1275 satellites per cell (2550 CMOS image sensors).

The encompassing data set was plotted as hourly aggregates after excluding a $10°$ by $10°$ box around the approximate center of SAA at $-25°$ latitude and $-55°$ longitude. The data were then plotted against external data from the Geostationary Operational Environmental Satellite (GOES) and Polar Operational Environmental Satellite (POES) spacecrafts to determine if there are any obvious correlations. Figure 14 shows data from GOES satellites (GOES-16, GOES-17, GOES-18) overlaid upon the Starlink CIS data. Figure 14a plots flares reported by any GOES satellite (with the flare class scaled to the approximate X-Ray flux). While the absolute variation in the Starlink CIS data over this time is not extreme, there does appear to be local maxima in the CIS data after the flares that occur around 15 December 2022 and 9 January 2023. Figure 14b plots the approximate ≥ 10 MeV and ≥ 50 integral proton fluxes. This is an approximation using a power-

law fit to the available differential proton effective energy and downsampled to the maximum value within a 30 minute span from GOES-16, GOES-17, or GOES-18. There is not a strong correlation observed, until some rise in CIS bright spot counts 10 January 2023, seemingly coincident with a rise in proton flux from GOES data. There is a similar increase on 13 January 2023. Figure 15 similarly shows data from the National Oceanic and Atmospheric Administration (NOAA) 19 polar orbiting satellite alongside Starlink CIS data. Figure 15a shows data from some of the omnidirectional
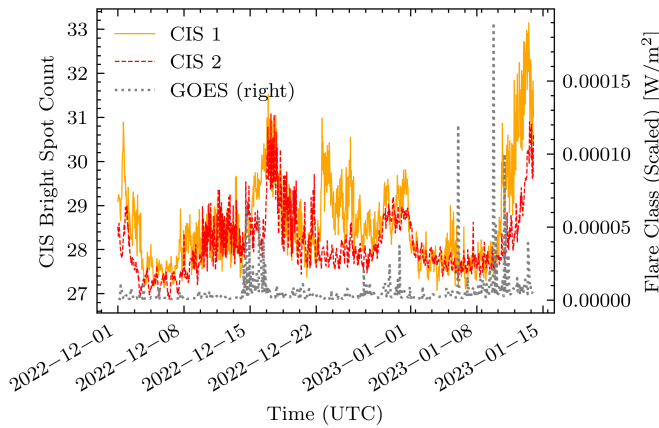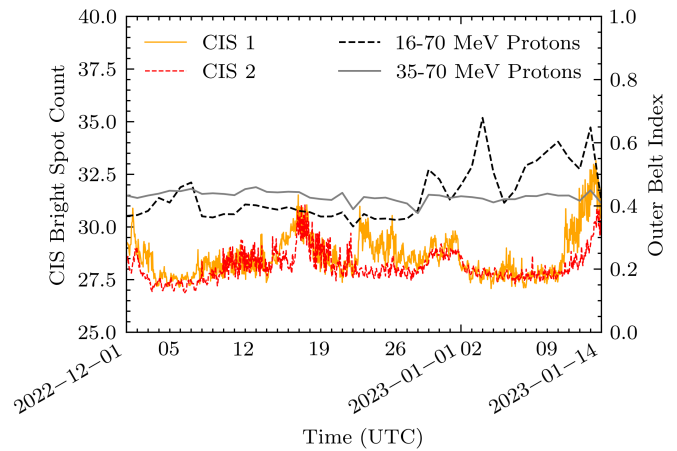
(a) Starlink CIS data vs. flares detected
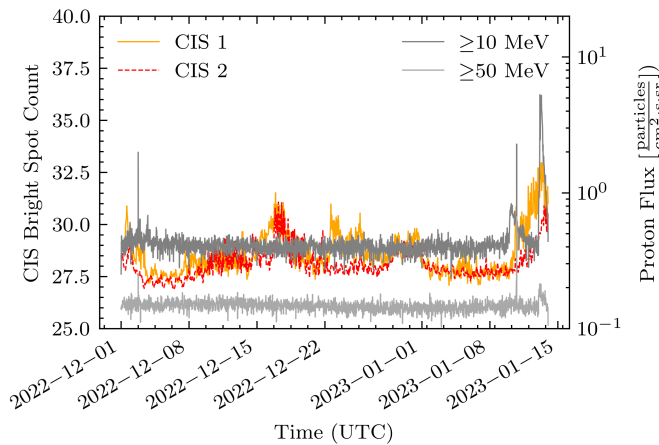
(b) Starlink CIS data vs. approximate ≥ 10 and ≥ 50 MeV integral proton flux

Fig. 14. Average global CIS bright spot counts from Starlink vs. data from GOES satellites

(a) Starlink CIS Data vs. POES Omnidirectional Proton Measurements

(b) Starlink CIS Data vs. POES >30 MeV Electron Data

Fig. 15. Average global CIS bright spot counts from Starlink vs. data from NOAA19 POES satellite
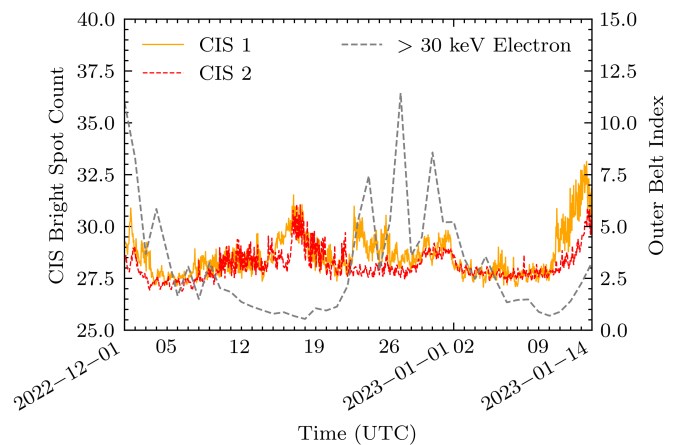
proton sensors. While there is a step change in the 16-70 MeV proton outer belt index shortly after 26 December 2022, there is not a corresponding change in the 35-70 MeV outer belt index indicating that there was not a significant change in the ≥ 35 MeV protons that would be expected to impact the CIS based on previous shielding analysis. Of interest, as seen in Figure 15b, there appeared to be some small variation coincident with changes in the >30 keV electron outer belt index.

The comparison to external data, notably to reported flares as well as the >30 keV electron outer belt index, provide some small indications that the Starlink CIS data could be used in a near real-time monitoring system of the LEO environment. However, future study is strongly suggested to better characterize the sensor and the expected response both via ground testing and comparison against more external data sources over longer time horizons that include multiple SPEs. Such work could enable the use of Starlink CIS to estimate particle flux rather than provide a relative measurement of the environment.

Overall, the observations from CMOS image sensors indicate they can be utilized to identify periods and locations of increased ionizing radiation. On-orbit data show that the

imager sensor registers higher rates of bright spots when passing over the South Atlantic Anomaly. Five minutes of data from the constellation is sufficient to outline the shape of the SAA enabling studies of the LEO environment on much shorter time scales than before. Additionally, it is shown that even with periods as short as a day, high spatial resolution can be achieved.

IV. CONCLUSION

Sensors on-board the Starlink constellation have proven capable of providing high spatiotemporal resolution of the LEO environment. The CMOS image sensors provide near real-time data during nominal and stormy solar conditions demonstrating potential for use as an environment monitoring system. Data accumulated with the TID sensors demonstrate the inherent conservatism of the dose calculations.

It is evident from this study that high quantities of COTS-based sensors can be leveraged to improve knowledge about the space environment. With improved characterization of existing sensors or added instrumentation to delineate sensor spot data by energy and ion species, high-resolution mapping and real-time observation of the space environment could be

further improved. Several additional follow-on studies could be applied to the data set reported herein.

V. Acknowledgement

VI. References

[1] T. Pultarova and E. Howell, "Starlink satellites: Everything you need to know about the controversial internet megaconstellation," 04 2022. [Online]. Available: https://www.space.com/spacex-starlink-satellites.html

[2] S. Lag, "Mega-constellation satellites on the horizon." [Online]. Available: https://www.dnv.com/to2030/technology/mega-constellation-satellites-on-the-horizon.html

[3] D. M. Fleetwood, P. S. Winokur, and P. E. Dodd, "An overview of radiation effects on electronics in the space telecommunications environment," *Microelectronics Reliability*, vol. 40, no. 1, pp. 17–26, January 2000. [Online]. Available: https://www.sciencedirect.com/science/article/pii/S0026271499002255

[4] H. C. Koons, J. E. Mazur, R. S. Selesnick, J. B. Blake, J. F. Fennell, J. L. Roeder *et al.*, "The Impact of the Space Environment on Space Systems," in *6th Spacecraft Charging Technology*, Nov. 1998, pp. 7–11.

[5] K. Mann, D. Holker, and N. Conn, "Responsive environmental assessment commercially hosted (REACH) payloads," in *2017 IEEE Aerospace Conference*, March 2017, pp. 3985–3990.

[6] C. L. Waters, B. J. Anderson, and K. Liou, "Estimation of global field aligned currents using the Iridium® system magnetometer data," *Geophysical Research Letters*, vol. 28, no. 11, pp. 2165–2168, June 2001. [Online]. Available: https://agupubs.onlinelibrary.wiley.com/doi/abs/10.1029/2000GL012725

[7] M. Cyamukungu, S. Benck, S. Borisov, G. Grégoire, J. Cabrera, J.-L. Bonnet *et al.*, "The energetic particle telescope (EPT) on board PROBA-V: Description of a new science-class instrument for particle detection in space," *IEEE Transactions on Nuclear Science*, vol. 61, no. 6, pp. 3667–3681, December 2014.

[8] T. P. O'Brien, W. R. Johnston, S. L. Huston, C. J. Roth, T. B. Guild, Y.-J. Su *et al.*, "Changes in AE9/AP9-IRENE version 1.5," *IEEE Transactions on Nuclear Science*, vol. 65, no. 1, pp. 462–466, January 2018.

[9] M. Xapsos, J. Barth, E. Stassinopoulos, S. Messenger, R. Walters, G. Summers *et al.*, "Characterizing solar proton energy spectra for radiation effects applications," *IEEE Transactions on Nuclear Science*, vol. 47, no. 6, pp. 2218–2223, December 2000.

[10] D. Heynderickx, B. Quaghebeur, E. Speelman, and E. Daly, *ESA's Space Environment Information System (SPENVIS) - A WWW interface to models of the space environment and its effects*. American Institute of Aeronautics and Astronautics, January 2000, p. 371. [Online]. Available: https://arc.aiaa.org/doi/abs/10.2514/6.2000-371

[11] C. Störmer, "Periodische Elektronenbahnen im Felde eines Elementarmagneten und ihre Anwendung auf Brüches Modellversuche und auf Eschenhagens Elementarwellen des Erdmagnetismus. Mit 32 Abbildungen." *Zeitschrift fuer Astrophysik*, vol. 1, p. 237, Jan. 1930.

[12] A. Tylka, J. Adams, P. Boberg, B. Brownstein, W. Dietrich, E. Flueckiger *et al.*, "CREME96: A revision of the cosmic ray effects on microelectronics code," *IEEE Transactions on Nuclear Science*, vol. 44, no. 6, pp. 2150–2160, December 1997.

[13] A. Varotsou, "OMERE space radiation environment and effects tool: new developments and new interface," March 2017. [Online]. Available: https://indico.esa.int/event/188/contributions/1622/attachments/1521/1753/OMERE_space_radiation_environment_and_effects_tool_Varotsou_07032017.pdf

[14] P. Pourrouquet, J.-C. Thomas, P.-F. Peyrard, R. Ecoffet, and G. Rolland, "FASTRAD 3.2: Radiation shielding tool with a new monte carlo module," in *2011 IEEE Radiation Effects Data Workshop*, Las Vegas, NV, USA, July 2011, pp. 200–204.

[15] M. Berger, "Stopping-powers and range tables for electrons, protons, and helium ions, NIST standard reference database 124," July 2017. [Online]. Available: http://www.nist.gov/pml/data/star/index.cfm

[16] T. D. Electronics. Teledyne e2v HiRel space sensor product line. [Online]. Available: https://www.teledynedefenseelectronics.com/e2vhrel/Documents/Teledyne%20Micro%20Dosimeter%20Presentation%20-%2016th%20April%202021.pdf

[17] M. Pérez, J. Lipovetzky, M. Sofo Haro, I. Sidelnik, J. J. Blostein, F. Alcalde Bessia *et al.*, "Particle detection and classification using commercial off the shelf CMOS image sensors," *Nuclear Instruments and Methods in Physics Research Section A: Accelerators, Spectrometers, Detectors and Associated Equipment*, vol. 827, pp. 171–180, August 2016. [Online]. Available: https://www.sciencedirect.com/science/article/pii/S0168900216302844

[18] V. Lalucaa, V. Goiffon, P. Magnan, G. Rolland, and S. Petit, "Single-event effects in CMOS image sensors," *IEEE Transactions on Nuclear Science*, vol. 60, no. 4, pp. 2494–2502, August 2013.

[19] Y. Cai, L. Wen, Y. Li, Q. Guo, D. Zhou, J. Feng *et al.*, "Single-event effects in pinned photodiode CMOS image sensors: SET and SEL," *IEEE Transactions on Nuclear Science*, vol. 67, no. 8, pp. 1861–1868, August 2020.

[20] G. Hopkinson, "Radiation effects in a CMOS active pixel sensor," *IEEE Transactions on Nuclear Science*, vol. 47, no. 6, pp. 2480–2484, December 2000.

[21] M. Cohen and J. David, "Radiation effects on active pixel sensors," in *1999 Fifth European Conference on Radiation and Its Effects on Components and Systems. RADECS 99 (Cat. No.99TH8471)*, Fontevraud, France, September 1999, pp. 450–456.

[22] S. Dhombres, A. Michez, J. Boch, F. Saigné, S. Beauvivre, D. Kraehenbuehl *et al.*, "Study of a thermal annealing approach for very high total dose environments," *IEEE Transactions on Nuclear Science*, vol. 61, no. 6, pp. 2923–2929, December 2014.

[23] S. Bourdarie, C. Inguimbert, J.-R. Vaille, P. Calvel, A. Sicard-Piet, D. Falguere *et al.*, "Benchmarking ionizing space environment models," in *2016 16th European Conference on Radiation and Its Effects on Components and Systems (RADECS)*, September 2016, pp. 185–188.